ARL-TR-10300 • MAR 2026

Producing Refractory High-Entropy Alloys with Cold Spray Additive Manufacturing

by Nickolas H. Sotiropoulos, Clara M. Mock,
Isaac M. Nault, Heather A. Murdoch, and Jack R. Summers

NOTICES

Disclaimers

The findings in this report are not to be construed as an official Department of the Army position unless so designated by other authorized documents.

The views and conclusions contained in this document are those of SURVICE Engineering and ARL. The U.S. Government is authorized to reproduce and distribute reprints for Government purposes notwithstanding any copyright notation here.

Citation of manufacturer's or trade names does not constitute an official endorsement or approval of the use thereof.

Destroy this report when it is no longer needed. Do not return it to the originator.

ARL-TR-10300 ● MAR 2026

Producing Refractory High-Entropy Alloys with Cold Spray Additive Manufacturing

Nickolas H. Sotiropoulos
SURVICE Engineering Company

Clara M. Mock, Isaac M. Nault, and Heather A. Murdoch
DEVCOM Army Research Laboratory

Jack R. Summers
Texas A&M University

REPORT DOCUMENTATION PAGE

1. REPORT DATE	2. REPORT TYPE	3. DATES COVERED	
		START DATE	END DATE
March 2026	Technical Report	7/24/24	9/15/25

4. TITLE AND SUBTITLE
Producing Refractory High-Entropy Alloys with Cold Spray Additive Manufacturing

5a. CONTRACT NUMBER	5b. GRANT NUMBER	5c. PROGRAM ELEMENT NUMBER
5d. PROJECT NUMBER	**5e. TASK NUMBER**	**5f. WORK UNIT NUMBER**

6. AUTHOR(S)
Nickolas H. Sotiropoulos, Clara M. Mock, Isaac M. Nault, Heather A. Murdoch, and Jack R. Summers

7. PERFORMING ORGANIZATION NAME(S) AND ADDRESS(ES)	8. PERFORMING ORGANIZATION REPORT NUMBER
DEVCOM Army Research Laboratory ATTN: FCDD-RLA-MD Aberdeen Proving Ground, MD 21005	ARL-TR-10300

9. SPONSORING/MONITORING AGENCY NAME(S) AND ADDRESS(ES)	10. SPONSOR/MONITOR'S ACRONYM(S)	11. SPONSOR/MONITOR'S REPORT NUMBER(S)

12. DISTRIBUTION/AVAILABILITY STATEMENT
DISTRIBUTION STATEMENT A. Approved for public release

13. SUPPLEMENTARY NOTES
ORCIDs: Nickolas H. Sotiropoulos, 0009-0009-0719-9984; Clara M. Mock, 0000-0001-8055-2371; Isaac M. Nault, 0000-0002-9597-9199; Heather A. Murdoch, 0000-0001-7710-0577; Jack R. Summers, 0000-0002-4739-9309

14. ABSTRACT
In this study, 15 different refractory high-entropy alloys were cold sprayed using blended elemental powders and subsequently heat treated. Alloys were analyzed in both the as-sprayed and heat-treated states, evaluating the underlying microstructures resulting from the process. The alloys were categorized as forming single-phase, two-phase, or multiphase structures after heat treatment. Most alloys were found to form uniform porosity throughout the bulk after heat treatment, although some maintained less than 1% porosity, with two alloys forming porosity that followed the interface of the cold spray layers. The goal of this study was to find chemistries that would effectively build up and form a dense single-phase microstructure after heat treatment. Of the 15 alloys evaluated, 3 alloys maintained less than 1% porosity after heat treatment and 5 alloys formed a single-phase microstructure. This study concluded that cold spray additive manufacturing offers a possible transition path to large-scale, high-entropy alloy production for certain alloy chemistries.

15. SUBJECT TERMS
refractory high-entropy alloys, cold spray, additive manufacturing, AM, Weapons Sciences

16. SECURITY CLASSIFICATION OF:			17. LIMITATION OF ABSTRACT	18. NUMBER OF PAGES
a. REPORT	b. ABSTRACT	C. THIS PAGE		
UNCLASSIFIED	UNCLASSIFIED	UNCLASSIFIED	UU	44

19a. NAME OF RESPONSIBLE PERSON	19b. PHONE NUMBER *(Include area code)*
Clara M. Mock	(520) 691-5149

STANDARD FORM 298 (REV. 5/2020)
Prescribed by ANSI Std. Z39.18

Contents

List of Figures v

List of Tables vi

Acknowledgments vii

1. Introduction 1

2. Methods 2

2.1 Materials 2

2.2 Cold Spray Process 3

2.3 Heat Treatment 4

2.4 Metallography 4

2.5 Characterization 5

3. Results 5

3.1 As-Sprayed Microstructure 5

3.2 Heat-Treated Microstructure 7

3.2.1 Porosity after Heat Treatment 8

3.2.2 Phase Structure after Heat Treatment 11

4. Discussion 15

4.1 Porosity 15

4.2 Homogenization 16

4.3 HfNbTaTi Alloy 18

4.4 Closing Remarks 19

5. Conclusions 20

6. References 21

Appendix. Scanning Electron Microscopy and Energy-Dispersive Spectroscopy Mapping of All Alloys **25**

List of Symbols, Abbreviations, and Acronyms **34**

Distribution List **35**

List of Figures

Figure 1. Heat-treated NbTaTiZr at a) 300× stitch and b) 500× (uniform porosity)..... 8
Figure 2. Heat-treated HfNbTaTiV at a) 300× stitch and b) 500× (interlayer porosity)..... 9
Figure 3. Heat-treated NbTaW at a) 300× stitch and b) 500× (fully dense).. 10
Figure 4. Microstructure a) as-sprayed and b) heat-treated single phase. 11
Figure 5. EDS mapping of HfNbTaTiV (single phase). 12
Figure 6. EDS mapping of MoTaZr (two-phase). 13
Figure 7. EDS mapping of NbTaW (multiphase). 14
Figure 8. CrMoNbV porosity..... 16
Figure 9. HfNbTaTi. 18
Figure 10. HfNbTaTiV secondary phase. 19
Figure A-1. NbTaW (multiphase). 26
Figure A-2. TaTiV (two-phase). 26
Figure A-3. HfTaZr (two-phase)..... 27
Figure A-4. MoTaZr (two-phase). 27
Figure A-5. HfMoNbTa (multiphase). 28
Figure A-6. HfNbTaTi (single-phase). 28
Figure A-7. NbTaTiV (single-phase). 29
Figure A-8. NbTaTiZr (single-phase). 29
Figure A-9. NbTiVW (multiphase)..... 30
Figure A-10. CrMoNbV (multiphase). 30
Figure A-11. HfNbTaTiV (single-phase)..... 31
Figure A-12. HfNbTaTiZr (single-phase). 31
Figure A-13. MoNbTaTiZr (two-phase). 32
Figure A-14. MoNbTaTiV (multiphase)..... 32
Figure A-15. NbTaTiVZr (two-phase)..... 33

List of Tables

Table 1. Elemental powders used and the corresponding size distributions. . 2
Table 2. RHEA alloys produced with CSAM. 3
Table 3. Spray conditions used to spray RHEA-blended powders. 4
Table 4. Porosity analysis. 6
Table 5. Heat-treated microstructure. 7
Table 6. Physical properties of the evaluated elements. 17

Acknowledgments

This research was performed in connection with contract/instrument W15P7T-19-D-0126 with the U.S. Army Combat Capabilities Development Command Army Research Laboratory.

1. Introduction

High-entropy alloys (HEAs) have recently been the focus of interest for extreme environments, such as reactor cores and turbine components. These alloys offer many exciting properties that make them well suited for these extreme applications, such as high strength,[1] fracture and fatigue resistance,[2–4] thermal stability,[5] irradiation resistance,[6] corrosion resistance,[7,8] and high-temperature oxidation resistance.[9,10]

HEAs are a new and rapidly developing alloy space in which alloys are composed of five or more different principle elements in equiatomic or near-equiatomic ratios.[11] Refractory HEAs (RHEAs) consist of alloys mostly made up of elements that have a high melting point from Groups IV, V, and VI on the periodic table, with some exceptions such as aluminum and silicon to improve oxidation performance. Refractory metals are typically defined as metals with a melting point above 2200 °C (4000 °F), specifically niobium, molybdenum, tantalum, tungsten, and rhenium, but some definitions include a broader selection of elements with a melting point above 1850 °C (3360 °F). This broader selection included titanium, vanadium, chromium, zirconium, hafnium, ruthenium, rhodium, osmium, and iridium.[12,13]

The most common production method for these alloys relies on arc melting,[14] induction melting, or mechanical alloying,[13] and although these methods are effective on a small scale, they often limit the geometric design of the material. Alternatively, additive manufacturing (AM) techniques offer a large range of geometric freedom, rapid prototyping, and reduced material waste compared with these traditional manufacturing techniques. Cold spray additive manufacturing (CSAM) offers many benefits to the traditional processing required for RHEAs such as large build volumes with very high deposition rates for rapid production. CSAM is a solid-state process as opposed to laser-powder bed fusion and direct energy deposition, avoiding the complicated thermal management of large builds that are typically seen in these other processes. The solid-state nature of the cold spray (CS) process makes it particularly suited to production of refractory metals because many of the difficult and costly steps within the fabrication process can be avoided because melting and hot isostatic pressing are not required.[15]

The purpose of this study was to determine whether CSAM could be used to produce high-density (low-porosity) single-phased solid solution RHEAs after heat treatment of the as-sprayed deposit. This would offer a transition path for large-scale RHEA and HEA production in a diverse range of shapes and geometries. In this study, pure elemental powders from Groups IV, V, and VI elements on the

periodic table (titanium, vanadium, chromium, zirconium, niobium, molybdenum, hafnium, tantalum, and tungsten) were chosen for the feedstock powders. This choice of using pure elemental feedstock powders rather than pre-alloyed HEA powder was due to the brittle nature of many of these HEAs at low temperature, presenting a significant obstacle to the CS process, which requires some level of ductility in the feedstock powders to effectively bond together and build up to a significant extent.[16,17] These elemental powders were combined in equal atomic ratios and sprayed together to form deposits, or samples, which were made up of these powders evenly distributed throughout the bulk. The combinations of these elemental powders were called blended elemental powders. After the powders were sprayed to form a deposit, they would be heat treated to induce diffusion of the component elements, forming the final HEA structure.

2. Methods

2.1 Materials

The RHEA alloys in this study were produced using elemental powders from different manufacturers but with an average particle size of less than 30 μm to maximize the speed the particles would achieve in the gas stream. The powders used in this study, as well as their size distributions, can be found in Table 1.

Table 1. Elemental powders used and the corresponding size distributions.

Material	Manufacturer	d10 (μm)	d50 (μm)	d90 (μm)
Cr	Exotech	9.85	23.87	39.81
Hf	Atlantic Equipment Engineers	5.90	10.09	14.97
Mo	H.C. Starck	12.31	23.16	35.13
Nb	Höganäs	7.85	15.48	25.07
Ta	Powders on Demand	7.61	12.11	17.04
Ti	H.C. Starck	8.61	19.51	33.55
W	Buffalo Tungsten	2.66	5.00	7.78
V	American Elements	1.17	2.93	5.73
Zr	American Elements	4.62	11.23	21.82

Before spraying, the elemental powders were blended in an equiatomic mixture using a Willy A. Bachofen CH-4005 type T2 C Turbula mixer (Willy A. Bachofen AG, Muttenz, Switzerland).

All alloys produced in this study can be found in Table 2. In choosing alloys to spray, it was important to pick alloys that would be conducive to the CSAM process. Elements like molybdenum and tungsten are brittle at room temperature, and although the gas temperature used was above the ductile to brittle transition

temperature for these elemental metals, the time in the gas stream was not enough to provide the required ductility to effectively deposit molybdenum and tungsten with this CS process.[18,19] Conversely, it is well established that titanium, niobium, and tantalum perform well in the CS process because their higher ductility allows for the material to undergo extreme deformation during the spray process.[20–24] Chromium has been established to be sprayable with the CS process but typically has poor deposition efficiencies and requires certain powder processing such as annealing to improve how well it sprays.[25,26] Impact innovations claim to be able to spray zirconium with their systems, achieving a high deposition efficiency and low porosity; otherwise, however, there is not much literature that can be found.[27] Similarly, not much can be found on pure vanadium and hafnium CS. Because they exhibit ductility at room temperature, it was assumed that, like chromium, they would be sprayable given the correct powder processing method. Based on what could be found in literature and prior cold spray experience, alloys were chosen that were expected to spray well. In choosing the alloys of interest for this study, any alloy containing both molybdenum and tungsten was avoided. It was also decided that every alloy sprayed in this study should contain, at the very least, either titanium, tantalum, or niobium to increase overall deposition efficiency since they are known to spray well.

Table 2. RHEA alloys produced with CSAM.

Carrier gas	Alloys		
	Three elements	**Four elements**	**Five elements**
Helium	NbTaW	HfMoNbTa	HfNbTaTiV
	TaTiV	HfNbTaTi	HfNbTaTiZr
		NbTaTiV	MoNbTaTiV
		NbTaTiZr	MoNbTaTiZr
		NbTiVW	NbTaTiVZr
Nitrogen	HfTaZr	CrMoNbV	. . .
	MoTaZr		

2.2 Cold Spray Process

The CS RHEA samples were produced using a VRC GEN III system, VRC Barrel applicator, and VRC nozzle 58 (VRC Metal Systems, Box Elder, South Dakota) attached to a Yaskawa Motoman MH50 robotic arm (Yaskawa Global, Fukuoka, Japan). The spray conditions used in this study can be found in Table 3. The spray conditions were chosen to determine whether the alloys would build up more effectively under a higher pressure or a higher temperature condition. Therefore, pressure and temperature for both conditions were chosen to accelerate a particle, of the same size and chemistry, to the same approximate velocity within the gas

steam. This would allow for a fair comparison between both helium conditions. A third condition, using nitrogen gas instead of helium gas, was used for three powders that showed indications of nozzle fouling or clogging. This nitrogen condition was chosen to allow for the material to be sprayed at lower impact velocities to limit buildup of material on the interior of the nozzle, preventing fouling. Samples were purposely sprayed so that the adhesion to the substate was poor, which allowed for easy removal of the material from the substate. This was achieved through using lower spray conditions and an AR500 substrate with a smooth surface finish and high surface hardness of approximately 50HRC. The sprayed material was removed from the substrate by wedging a razor blade into the deposit/substrate interface and striking with a hammer.

Table 3. Spray conditions used to spray RHEA-blended powders.

Spray condition	Carrier gas	Pressure (psi)	Temperature (°C)	Powder feed rate (rpm)	Standoff distance (mm)	Nozzle transverse speed (mm/s)
High temperature	He	425	500	8	25	200
High pressure	He	525	350	8	25	200
Decreased fouling (nitrogen)	N2	800	650	8	25	200

2.3 Heat Treatment

Samples were evaluated under two conditions: the as-sprayed and heat-treated conditions. Samples were placed in a Carbolite Gero 1600 °C Tube Furnace TF1 16/100/450 and then heated to 1500 °C where they were held for 4 h. During the heat treatment, the furnace was continuously purged using high purity argon to prevent contamination from oxygen and other reactive gases. The heat treatment was chosen to maximize the driving force for diffusion through setting the temperature to the maximum safe operating temperature for the tube furnace.

2.4 Metallography

Metallographic specimens were prepared by using a Struers CitoPress-20 and a Struers LaboForce-100 automatic polisher (Struers ApS, Ballerup, 2750 Copenhagen, Denmark). Samples were mounted for evaluation along the build direction and polished to a 0.04-μm finish. During the polishing process, special consideration was taken to minimize pullout in the samples. Pads were selected based on which ones would minimize material pullout according to the vendors' suggestions.

2.5 Characterization

Optical cross-sectional images used for image analysis were obtained using a Keyence VHX-7000 (Keyence Corp., Itasca, Illinois) optical microscope at 300× magnification. The optical images of the samples were subsequently analyzed using the image processing package Fiji to get an estimate of the levels of porosity.[28] By carefully thresholding the entire cross section of each sample, the area of the internal porosity was calculated and then compared to the total area. Energy-dispersive spectroscopy (EDS) was performed on each sample using a Phenom XL SEM (Thermo Fisher Scientific Inc., Waltham, Massachusetts). EDS elemental mapping analysis was used to determine the level of diffusion in the sample through comparison of the as-sprayed samples and the heat-treated samples. Powder size analysis on all the feedstock powders was preformed using a Partica LA-960V2 laser scattering particle size distribution analyzer (HORIBA Ltd., Kyoto, Japan).

3. Results

3.1 As-Sprayed Microstructure

Inspecting the samples in the as-sprayed condition acted as the baseline for the HEA samples. HfTaZr, MoTaZr, and CrMoNbV showed indication of nozzle fouling and clogging, and so they were sprayed using the lower nitrogen condition. Of the RHEAs sprayed using helium gas, NbTaW was the only mixture that built up under only one condition, which was the high-pressure condition. This may be attributed to the high temperature performance of the individual elemental powder constituents. Due to the high melting points of these elements, the spray temperature may not have had enough softening effect on these powders to allow for good deformation during the spray process in the lower-pressure condition. Therefore, for the NbTaW RHEA, a high-pressure condition may be required to obtain sufficient deposition of this alloy.

The performance of each alloy in a particular spray condition was determined by the level of porosity within the as-sprayed deposit. A lower porosity in the as-sprayed deposit was taken to indicate that the blended powder deposited more efficiently with either the higher temperature, or higher-pressure spray condition. HfMoNbTa, HfNbTaTi, NbTaTiV, NbTiVW, HfNbTaTiZr, MoNbTaTiV, and MoNbTaTiZr performed better when sprayed at a higher temperature compared with their higher-pressure alternatives. It is important to note that for MoNbTaTiZr, the as-sprayed porosity in the high temperature condition was lower, but after heat treatment, the porosity increased much more significantly than it did for the high-pressure sample of the same chemistry. NbTaW, TaTiV, NbTaTiZr, HfNbTaTiV,

and NbTaTiVZr performed better in the high-pressure condition. HfNbTaTiV had a slightly lower as-sprayed porosity in the high-pressure condition, but after heat treatment, the porosity in the high temperature condition was lower. This increase in porosity may be the result of many factors, including pullout during polishing of both the as-sprayed and heat-treated samples. This seems to be especially likely because the increase in porosity is so minimal. A full list of the porosity analysis can be found in Table 4.

Table 4. Porosity analysis.

Alloy	Spray conditions	Analysis condition	Optical porosity (%)	Change in porosity (%)
HfTaZr	Decreased fouling (nitrogen)	As-sprayed	0.453	
		Heat-treated	1.514	1.062
MoTaZr	Decreased fouling (nitrogen)	As-sprayed	1.461	
		Heat-treated	0.810	−0.651
NbTaW	High pressure	As-sprayed	0.330	
		Heat-treated	0.052	−0.278
TaTiV	High temperature	As-sprayed	0.294	
		Heat-treated	2.059	1.766
	High pressure	As-sprayed	0.202	
		Heat-treated	1.576	1.374
CrMoNbV	Decreased fouling (nitrogen)	As-sprayed	1.596	
		Heat-treated	19.070	17.474
HfMoNbTa	High temperature	As-sprayed	0.077	
		Heat-treated	0.224	0.147
	High pressure	As-sprayed	0.232	
		Heat-treated	3.996	3.764
HfNbTaTi	High temperature	As-sprayed	0.069	
		Heat-treated	1.193	1.124
	High pressure	As-sprayed	0.050	
		Heat-treated	2.923	2.873
NbTaTiV	High temperature	As-sprayed	0.498	
		Heat-treated	1.538	1.040
	High pressure	As-sprayed	0.629	
		Heat-treated	1.740	1.110
NbTaTiZr	High temperature	As-sprayed	2.714	
		Heat-treated	15.037	12.322
	High pressure	As-sprayed	0.095	
		Heat-treated	8.558	8.464
NbTiVW	High temperature	As-sprayed	5.851	
		Heat-treated	2.622	−3.229
	High pressure	As-sprayed	27.483	
		Heat-treated	4.712	−22.771
HfNbTaTiV	High temperature	As-sprayed	0.072	
		Heat-treated	2.604	2.532
	High pressure	As-sprayed	0.025	
		Heat-treated	3.570	3.546

Table 4. Porosity analysis (continued).

Alloy	Spray conditions	Analysis condition	Optical porosity (%)	Change in porosity (%)
HfNbTaTiZr	High temperature	As-sprayed	0.273	
		Heat-treated	9.707	9.434
	High pressure	As-sprayed	0.682	
		Heat-treated	11.558	10.876
MoNbTaTiV	High temperature	As-sprayed	11.404	
		Heat-treated	3.231	−8.174
	High pressure	As-sprayed	14.895	
		Heat-treated	2.848	−12.047
MoNbTaTiZr	High temperature	As-sprayed	8.325	
		Heat-treated	17.991	9.666
	High pressure	As-sprayed	10.039	
		Heat-treated	3.267	−6.771
NbTaTiVZr	High temperature	As-sprayed	5.976	
		Heat-treated	10.243	4.267
	High pressure	As-sprayed	0.450	
		Heat-treated	9.854	9.404

3.2 Heat-Treated Microstructure

The heat-treated microstructure can be categorized into how porosity formed and the number of phases present within the heat-treated deposits. The resulting porosity in the samples can be categorized as follows: uniform porosity, linear porosity, and little to no porosity. The phases present within the samples were similarly grouped together into three categories. These categories were as follows: more than two phases (multiphase), two phased, or single-phased homogeneous. Table 5 outlines the microstructure of all the alloys evaluated in this study.

Table 5. Heat-treated microstructure.

Phase structure	Porosity		
	Uniform porosity	Interlayer porosity	Fully dense
Single-phase	NbTaTiV NbTaTiZr		
		HfNbTaTi	
		HfNbTaTiV	
	HfNbTaTiZr		
Two-phase	HfTaZr		
			MoTaZr
	TaTiV MoNbTaTiZr NbTaTiVZr		
Multiphase			NbTaW
	CrMoNbV NbTiVW		
			HfMoNbTa (low pressure)
	MoNbTaTiV		

3.2.1 Porosity after Heat Treatment

Porosity was formed uniformly during heat treatment, likely as a result of the Kirkendall effect.[29] This increase in porosity may also be attributed to the melting of certain binary or higher-order compounds. For example, Cr-Ti, Cr-Zr, Hf-V, and V-Zr have all been reported to have a liquidus below the sintering temperature used in this work.[30–32] The formation of a liquid phase during heat treatment could have caused volume expansion followed by crack and/or pore formation.

The most common category of porosity across all samples was uniform porosity. This was the most common of the microstructures seen within the heat-treated samples and is visible in Figure 1, where a large volume of porosity is evenly distributed throughout the bulk of the material without order. This uniform large-scale porosity was seen across different chemistries with varying levels of as-sprayed porosity.

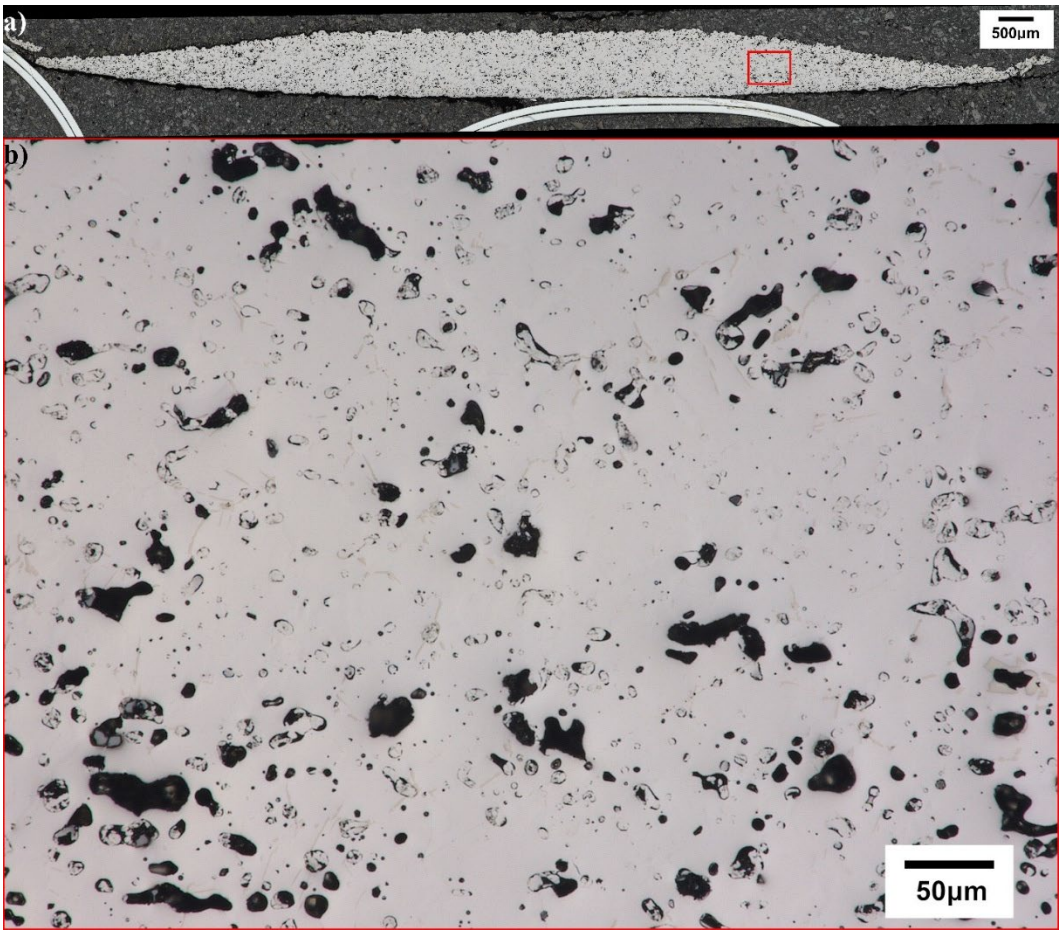

Figure 1. Heat-treated NbTaTiZr at a) 300× stitch and b) 500× (uniform porosity).

Interlayer porosity was much less common among the evaluated samples and was only seen in HfNbTaTi and HfNbTaTiV, which can be seen in Figure 2. This porosity typically followed the darker phase clearly seen in Figure 2b. This is likely due to some factor during the spray process leading to the buildup of gases at the interface between layers. This may be the result of moisture or any of the gases, specifically oxygen, nitrogen, and/or hydrogen, present on the surface of powders. During heat treatment, these gases are desorbed from the powders at elevated temperatures. Once released, it is hypothesized that these gases would migrate to the interface between two layers because the mechanical bonding between two separate layers tends to be weaker than the bonding seen within the same CS layer.[33] Another possibility is that this interlayer porosity may be the result of oxidation or nitriding during the CS process as the hot surface of a new CS layer is exposed to atmosphere.

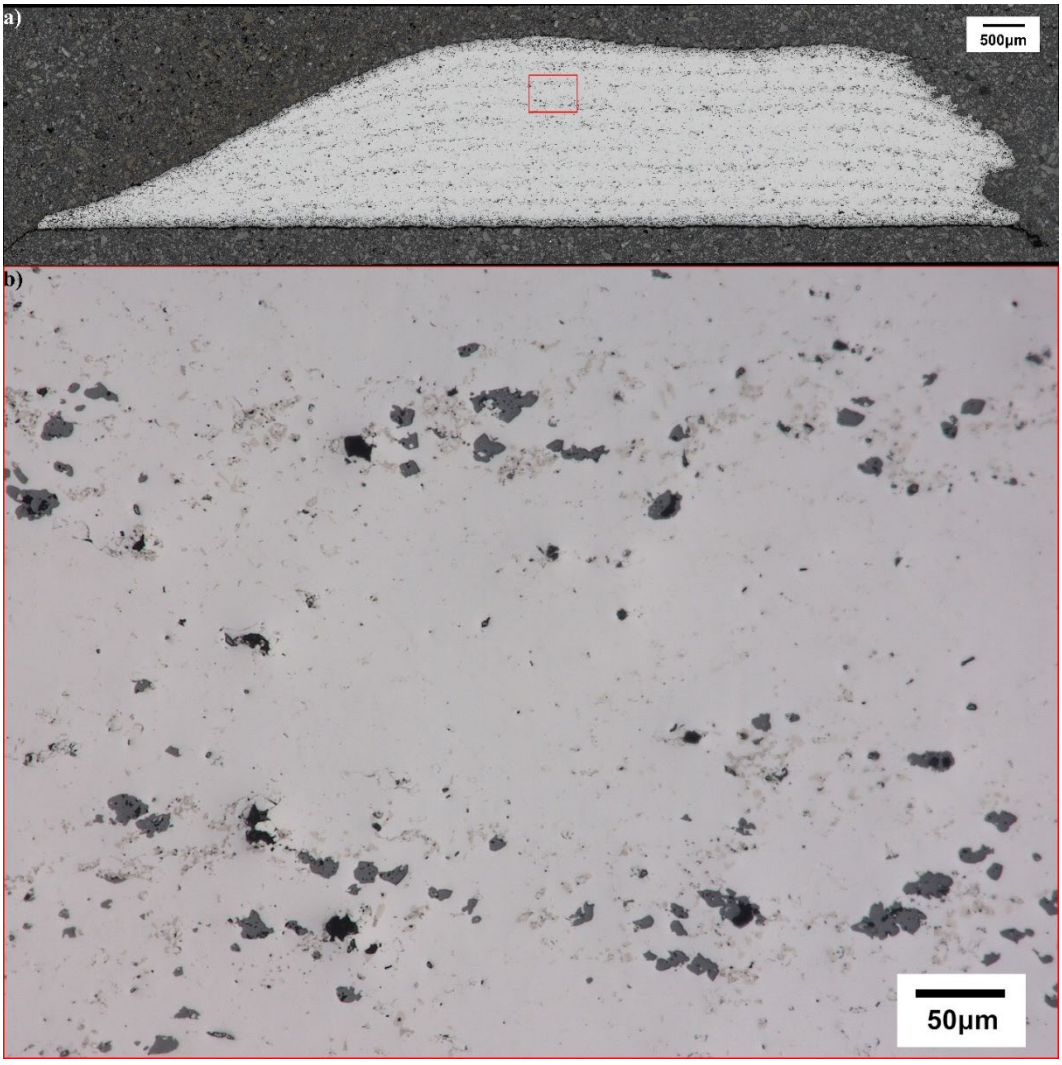

Figure 2. Heat-treated HfNbTaTiV at a) 300× stitch and b) 500× (interlayer porosity).

There is also a possibility that the porosity following the layer lines is instead pullout of the secondary phase after polishing. This would be supported by the idea that both the secondary phase and the porosity appear in relatively the same area of the sample, as well as both appearing to be similar in size. In this case, both HfNbTaTi and HfNbTaTiV would be more accurately classified as having uniform porosity that is very close to being fully dense.

A few of the RHEAs evaluated demonstrated fully dense (99%+) microstructures when heat treated. As seen in Table 5, the only RHEAs with <1% porosity after heat treatment were MoTaZr, NbTaW, and HfMoNbTa in the low-pressure condition. Of the samples with low porosity, NbTaW had an extremely dense microstructure in both the as-sprayed and heat-treated conditions. The NbTaW microstructure can be seen in Figure 3. Both MoTaZr and NbTaW demonstrated a decrease in porosity after heat treatment.

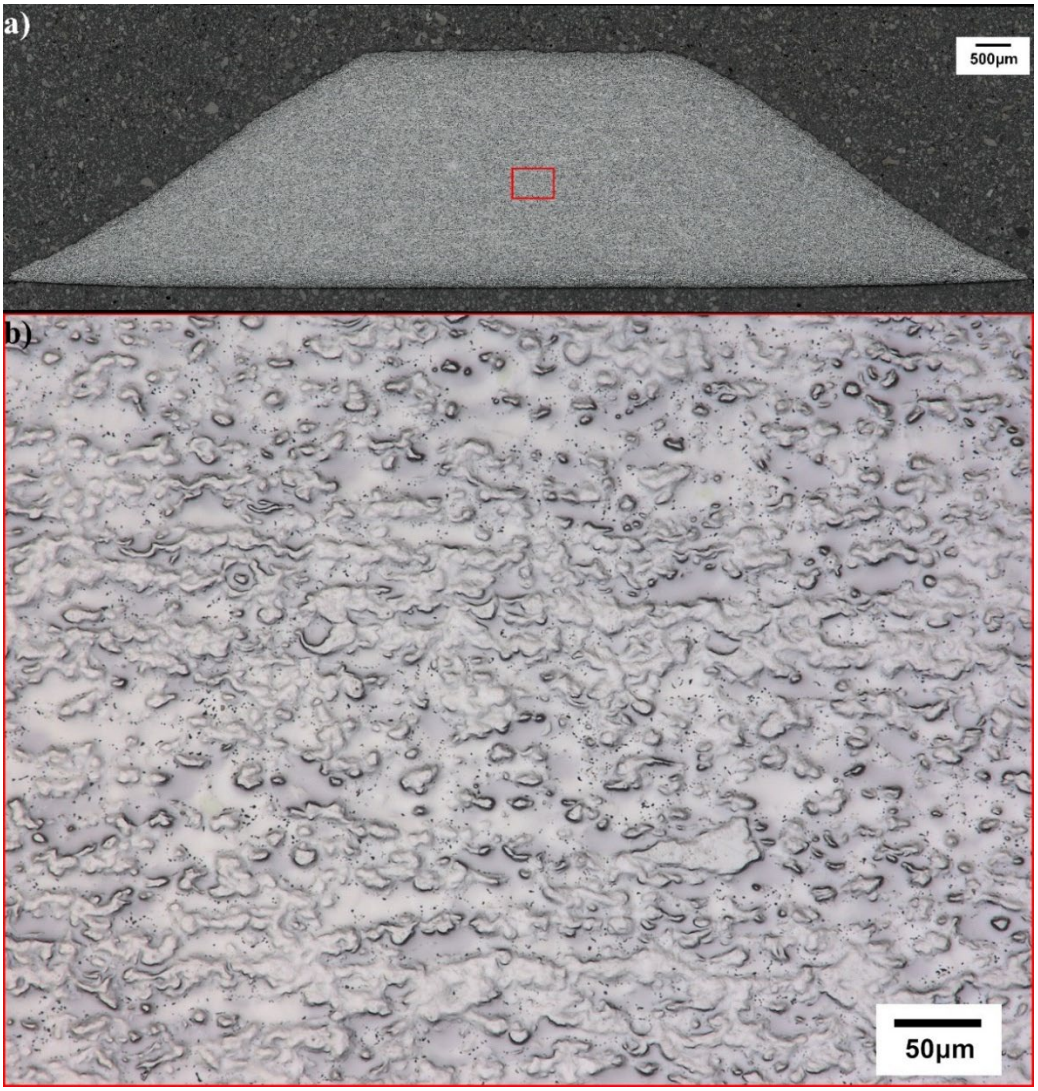

Figure 3. Heat-treated NbTaW at a) 300× stitch and b) 500× (fully dense).

3.2.2 Phase Structure after Heat Treatment

The distribution of chemistry of the heat-treated RHEA CS deposits was measured using EDS comparing the as-sprayed microstructure of the samples with the microstructure after heat treatment. The difference in the microstructure between the as-sprayed and heat-treated state for the same alloy can be seen in Figure 4. Analysis was only performed on the number of phases present and the approximate ratio of elemental constituents. Data on the crystal structure present and exact phases present within the deposits will be performed in later studies, because the focus here was to establish a starting point for RHEA chemistries that may favor the CS process.

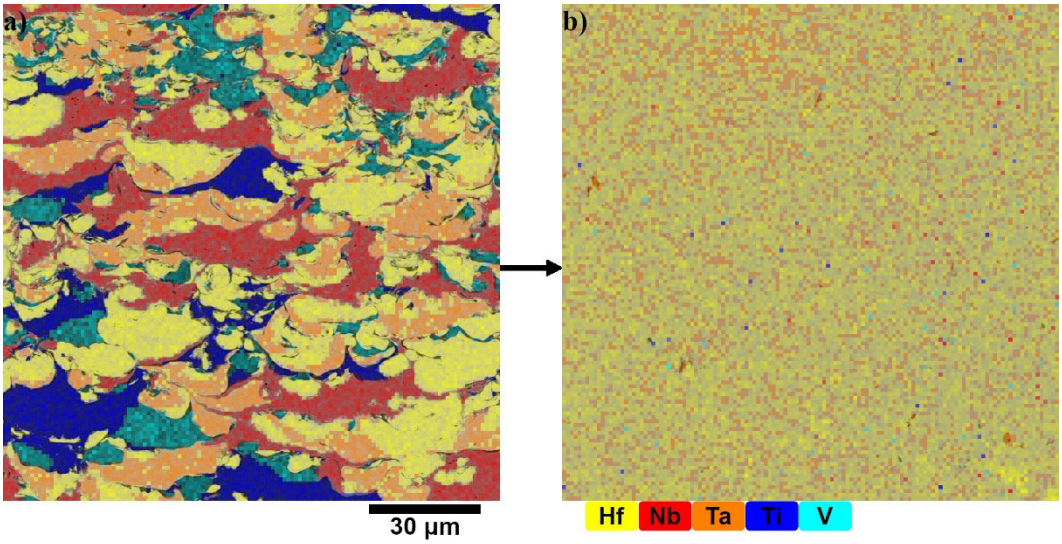

Figure 4. Microstructure a) as-sprayed and b) heat-treated single phase.

All samples were categorized into three groups after heat treatment: single-phase, two-phase, or multiphase. These categories did not perfectly describe every alloy evaluated in this study, but they were intended to categorize them to determine any trends between similar material systems. Because pores, voids, and inclusions were common and unavoidable in many cases, they were largely ignored when considering the phase structure of the matrix material. Within these categories, the compositions all had similar microstructures after heat treatment, with minimal differences. Of the evaluated RHEAs, NbTaTiV, NbTaTiZr, HfNbTaTi, HfNbTaTiV, and HfNbTaTiZr formed a single phase during the heat treatment. It is interesting to note that all alloys that formed a single solution involved the NbTaTi system. A representative EDS map can be seen in Figure 5. All single-phased alloys were identified by the uniform distribution of elements within the EDS mapping.

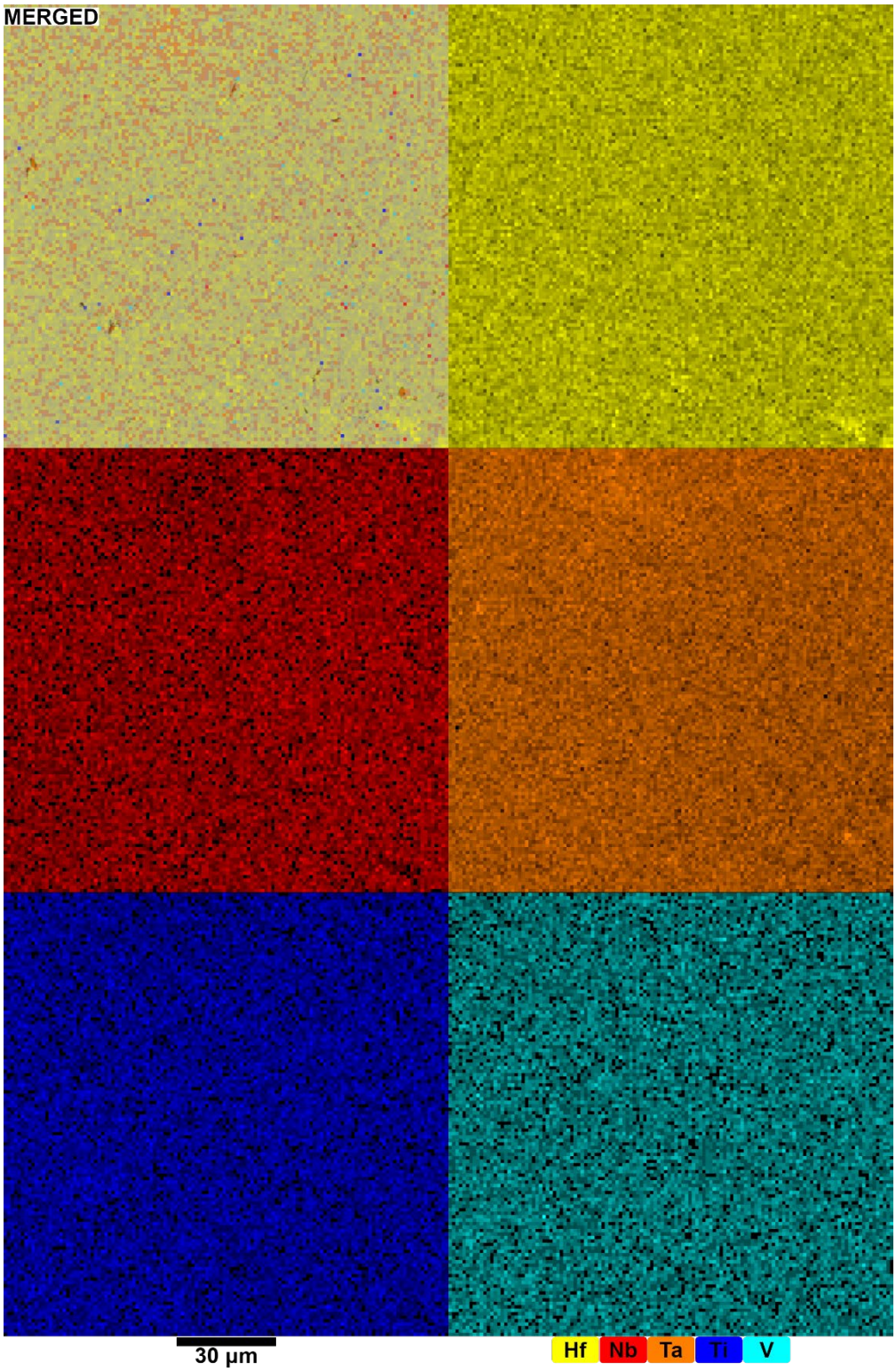

Figure 5. EDS mapping of HfNbTaTiV (single phase).

Five of the CS deposits were found to form a two-phase structure when evaluated under EDS analysis. The EDS analyses for HfTaZr, MoTaZr, TaTiV, NbTaTiVZr, and MoNbTaTiZr show two different obvious phases, like the EDS map seen in Figure 6. Although at first glance the MoNbTaTiZr and NbTaTiVZr alloys produced via CSAM, and subsequent heat treating, may appear to have formed a single-phased homogeneous structure, note that the grains are composed of a fine lamellar structure. Scanning electron microscopy (SEM) and EDS mapping of MoNbTaTiZr and NbTaTiVZr, as well as all the alloys investigated in this study, can be found in the Appendix.

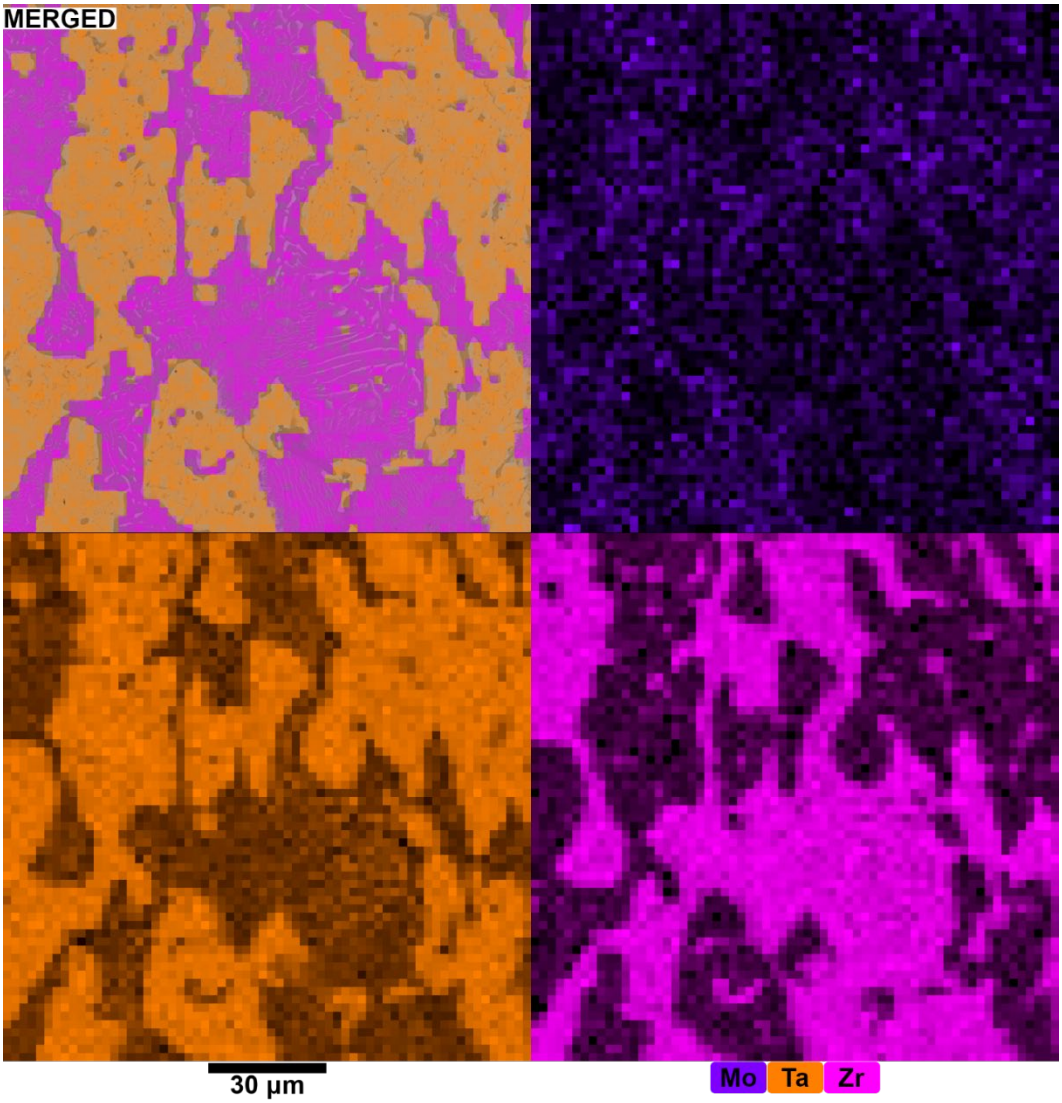

Figure 6. EDS mapping of MoTaZr (two-phase).

Alloys like HfNbTaTi, HfNbTaTiV, NbTaTiVZr, and TaTiV were found to have individual elemental pockets within the bulk of the material, but HfNbTaTi and HfNbTaTiV were both categorized as single-phased, whereas NbTaTiVZr and

TaTiV were categorized as two-phased. The difference in categorization was due to the size scale and distribution of these individual elemental pockets. For HfNbTaTi and HfNbTaTiV, these inclusions appeared in isolated pockets in specific locations within the samples. Moreover, for the most part, 134- × 134-μm squares, like those seen in Figures 5–7 could be captured avoiding these inclusions. Alternatively, the inclusions found in NbTaTiVZr and TaTiV were much smaller, evenly distributed, and were found throughout the bulk to the point where it was difficult to find areas within the cross section that did not have these phases.

Some alloys did not achieve sufficient diffusion from the heat treatment performed on the deposit leading to a non-uniform microstructure with pockets of pure elements like what was seen in the as-sprayed condition. As seen in Figure 7, tungsten seems to show very minimal diffusion, with the NbTaW system showing the least amount of overall diffusion between the consolidated elemental powders. It would be interesting to test the mechanical and thermal properties of these metal matrix composites because the materials may demonstrate unique properties.

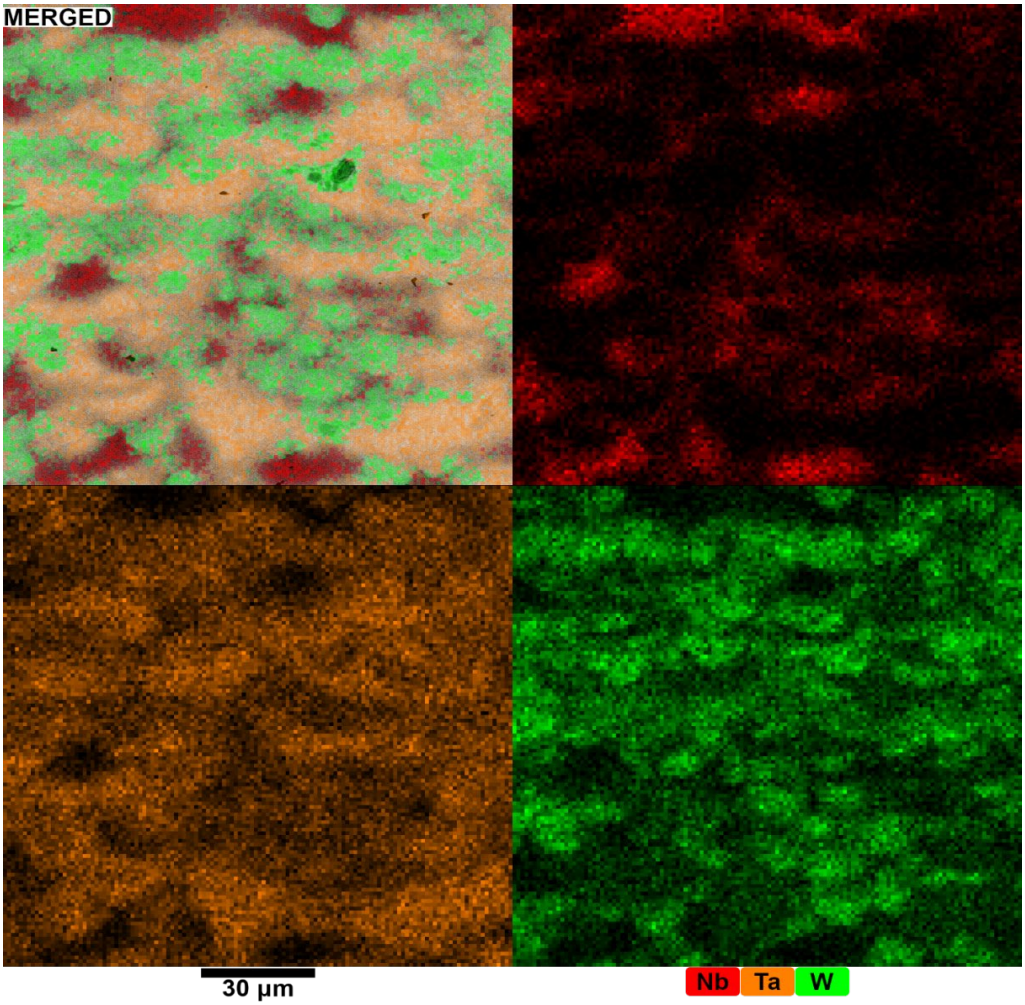

Figure 7. EDS mapping of NbTaW (multiphase).

4. Discussion

4.1 Porosity

Evaluating the change in porosity from the as-sprayed condition to the heat-treated condition did not lead to an obvious trend for any individual alloy systems (Table 5). Some samples, like HfMoNbTa and NbTaW, were fully dense in both the as-sprayed and heat-treated state. Other samples, like HfNbTaTiV, NbTaTiV, and the high-pressure NbTaTiZr, were fully dense in the as-sprayed condition, but they significantly increased porosity after heat treatment. This indicates that a fully dense as-sprayed deposit does not guarantee a fully dense structure after heat treatment. The high-pressure NbTiVW sample, which had approximately 27.5% porosity in the as-sprayed condition, decreased to 4.7% porosity after heat treatment, showing that in some cases, porosity would even decrease after heat treatment. This indicates that predicting how porosity will evolve in blended elemental CSAM RHEAs will not be exclusively dependent on the elemental constituents or the as-sprayed density of the deposit. Evaluating a larger sample size may lead to a connection between alloy chemistry and pore evolution, but no conclusive trend could be drawn from the limited sample size evaluated in this study. The Kirkendall effect is likely to play a large role in the formation of porosity within these materials, and further research is needed to create a road map on how these complex elemental systems interact with each other.

A significant factor that will affect the resulting properties of these alloys is the powder processing and contamination within the feedstock materials. As seen in the CrMoNbV sample shown in Figure 8, there is a significant level of what appears to be gas porosity. This porosity may be the result of off-gassing of the powder during the heat treatment process. After heat treatment, CrMoNbV showed an increase in porosity of 17.474%. This was the most significant increase in porosity for any sample evaluated. Because this was the only chemistry involving chromium, it is possible that the chromium feed stock powder had a significant level of moisture that evolved into a gas during heat treatment, creating excessive gas porosity through the bulk of the material.[34] However, it is possible that this may have been an extreme example of the Kirkendall effect and not gas porosity.

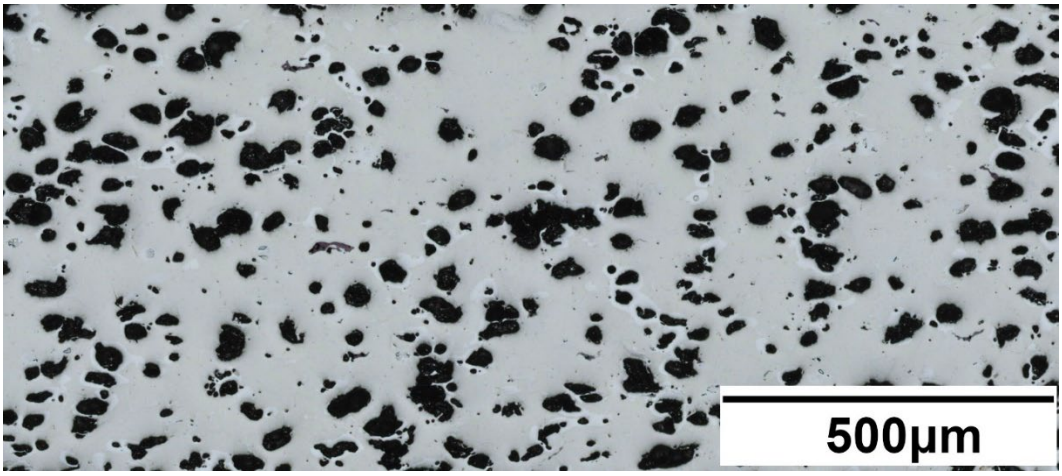

Figure 8. CrMoNbV porosity.

MoTaZr, NbTaW, NbTiVW, MoNbTaTiV, and MoNbTaTiV sprayed under the high-pressure condition were the only samples that showed a decrease in porosity after heat treatment. Of the five alloys that decreased in porosity, MoTaZr is the only alloy that showed significant diffusion between powders. This effective diffusion, coupled with the low final porosity, may make MoTaZr a good candidate for further evaluation. HfNbTaTi and HfNbTaTiV would also be valuable alloys to examine in future studies because they are the two samples that demonstrated the interlayer porosity. Because this porosity seemed to follow the interface between individual CS layers, it may not be a result of the diffusion during heat treatment, and it may even be mitigated or removed through adapting the CS process. Furthermore, after heat treatment, HfNbTaTi had a very high density and homogenized into a single phase, making it a strong candidate to continue to study.

4.2 Homogenization

Of all the alloys investigated in this study, only those containing niobium, tantalum, and titanium formed single-phased solid solutions when analyzed using EDS analysis. This success seen among niobium, tantalum, and titanium may be related to the ease of spraying with these materials. The extreme deformation that niobium, titanium, and tantalum experience during CS increases the surface area of the particles, providing greater surface areas and increasing rate of diffusion during heat treatment.

When considering the homogeneity of these alloys, it is important to discuss the Hume–Rothery rules. It has been established that the Hume–Rothery rules are not fully applicable to HEAs because it does not adequately explain how elements of different crystal structures come together to form one single-phase solid solution as established by Guo and Liu.[35] The Hume–Rothery rules outline a basic criterion for

two elements to form a solid solution based on the element's atomic radii, crystal structure, valence, and electronegativity. The necessary values for each element evaluated in this study are listed in Table 6. Based on the values in Table 6, one could expect the NbTaW system to have homogenized better than it did. Instead, it seems that, at least for the sake of CS alloys, those that are composed of more effectively sprayed materials, like niobium, tantalum, or titanium, make the best RHEAs for CS. This can likely be attributed to these elemental powders having the highest as-sprayed density and the most significant deformation on impact, improving the overall diffusion through increasing surface area and particle-to-particle contact. This can be seen in how the NbTaTi system seemed to operate the most effectively in terms of forming dense as-sprayed deposits that homogenized during heat treatment without forming significant levels of porosity in the process.

Table 6. Physical properties of the evaluated elements.[36]

Element	Atomic radii (pm)	Crystal structure	Valency	Electronegativity
Cr	166	BCC	6	1.66
Hf	208	HCP	4	1.30
Mo	190	BCC	6	2.16
Nb	198	BCC	5	1.60
Ta	200	BCC	5	1.50
Ti	176	HCP	4	1.54
W	193	BCC	6	2.36
V	171	BCC	5	1.63
Zr	206	HCP	4	1.33

It was also found that tungsten and molybdenum were slow diffusers that would often form multiphase alloys. Both tungsten-containing alloys, NbTaW and NbTiVW, formed multiphase alloys, and so it was hypothesized that tungsten acted as a slow diffuser that prevented or decreased the diffusion of the other alloying elements. This is especially evident in the NbTaW sample, because in many other alloys niobium and tantalum effectively diffused and homogenized with the other constituents, whereas in this alloy they tended to stay within localized pockets. In the NbTiVW alloy, the tungsten seemed to diffuse more effectively than in the NbTaW alloy, which may indicate that the vanadium helps to improve the diffusion. Molybdenum seemed to also act as a slow diffuser, as seen in HfMoNbTa, CroMoNbV, and MoNbTaTiV, which all formed multiphased alloys, although the molybdenum in MoNbTaTiZr and MoTaZr seemed to diffuse much more readily, which may indicate that zirconium helps to promote diffusion of molybdenum, similar to how vanadium may help to improve the diffusion of tungsten.

4.3 HfNbTaTi Alloy

Of all the alloys evaluated, the most promising chemistry based on the heat-treated microstructure is HfNbTaTi (Figure 9). Although this alloy was found to have more than 1% total porosity, it was not significantly more, with only 1.193% total porosity after heat treatment. In Figure 9, there is a significant amount of a secondary phase that, similarly to the porosity, follows the layer lines.

Figure 9. HfNbTaTi.

This secondary phase was omitted from the porosity analysis using the thresholding function in Fiji.[28] It is hypothesized that this phase can be mitigated through a specialized heat treatment, spraying in an inert environment, and improvement to the spray process and feedstock powders. HfNbTaTi was also one of the five alloys to form a single-phased solid solution after heat treatment. Although this does not exactly fulfill the requirements outlined at the beginning of this work of a high-density, single-phased solid solution RHEA, it is only a fraction of a percent away. The way the porosity in HfNbTaTi and HfNbTaTiV follows along the layer lines seems to indicate that this porosity is not necessarily a biproduct of the Kirkendall effect during diffusion, but instead it is a product of either the heat treatment or the spray process. If it was the result of different diffusion rates, then the porosity would be evenly distributed throughout the bulk like many of the other samples. Instead, the pores and secondary phase congregate at the layer interfaces, which is not fully understood. As stated in Section 3.2.1, there is also a chance that this porosity at the inface is just the result of pullout of this secondary phase. This would still make HfNbTaTi and HfNbTaTiV worthwhile alloys to evaluate in further studies.

The secondary phase seen throughout the bulk of the HfNbTaTi and HfNbTaTiV samples was hypothesized to be hafnium oxide (HfO_2). EDS of these phases was used to confirm they were largely composed of hafnium, as seen in Figure 10. The large hafnium-rich area along the top of the sample in Figure 10 was in contact with the alumina (Al_2O_3) boat during heat treatment. At 1500 °C, hafnium has a lower

free energy than aluminum, which seems to have resulted in the hafnium reducing the Al_2O_3 boat.[37] Because this surface phase appears to be very similar to the secondary phases seen throughout the bulk, it was hypothesized that they were also HfO_2, resulting from either 1) entrapped oxygen gas or oxides within or 2) on the surface of the other powders used to spray the alloy. This phase is not seen in alloys containing both hafnium and zirconium. ZrO_2 has a lower free energy than HfO_2 at all temperatures according to the Ellingham diagram. Therefore, it is hypothesized that the addition of zirconium to RHEAs containing hafnium may help to limit the formation of HfO_2 that forms at the layer interface. This makes a case to also evaluate the alloy HfNbTaTiVZr in future studies, because the addition of zirconium may help to stabilize the hafnium and prevent the formation of these oxides.

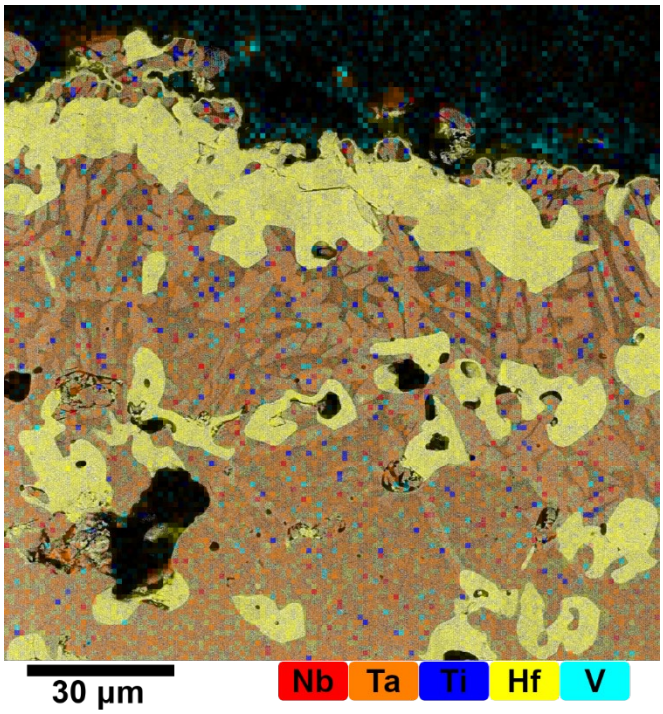

Figure 10. HfNbTaTiV secondary phase.

4.4 Closing Remarks

There is still a significant breadth of research needed to improve our understanding of this complex alloys' space; however, based on the data, CSAM does offer a transition path to produce large-scale RHEA parts with a fast build rate. As was established in this work, this process is chemistry-dependent and is not suitable for all RHEAs. Significant work is needed to further explore which chemistries work well in the CSAM process and determine if heat treatments can be improved to maximize diffusion while minimizing the formation of porosity. Work is also

required to improve the feed stock powder and system used for the method. It is critical to limit contamination in the feedstock powders. Including a powder pre-heater may help to improve the deposition of molybdenum and tungsten through heating the powders to above the ductile to brittle transition temperature. Once a successful chemistry is determined, work will be required to perfect the exact blending ratio of powders to consistently produce alloys of the same atomic makeup. Although this manufacturing method is far from mature, it offers a path to producing these alloys on a large scale in a much more practical and feasible method than any of the other established methods.

5. Conclusions

Fifteen different CSAM RHEAs chemistries were manufactured and heat treated. Of these 15 chemistries:

- Three chemistries, MoTaZr, NbTaW, HfMoNbTa, maintained less than 1% percent porosity after heat treatment.
- Five chemistries, NbTaTiV, NbTaTiZr, HfNbTaTi, HfNbTaTiV, and HfNbTaTiZr, formed single-phased homogeneous structures.
- HfNbTaTi and HfNbTaTiV may be good candidates for further studies. They both formed a single-phased solid solution after heat treatment and had relatively low porosity. Although this porosity was more than the 1%, it was unusual because it seemed to follow the cold spray layer lines, unlike the other samples that formed significant porosity throughout the bulk without an obvious pattern.
- HfNbTaTiVZr may also be worth investigating because the zirconium may help to stabilize the hafnium, preventing the formation of the secondary phases seen in both HfNbTaTi and HNbTaTiV.

CSAM offers an efficient transition path to manufacturing large-scale, complex geometry RHEA components within a short lead time. This manufacturing method is certainly material-dependent but offers a more economical and sustainable approach than traditional methods, like arc and induction melting.

6. References

1. Wu S, Qiao D, Zhao H, Wang J, Lu Y. A novel NbTaW0.5 (Mo2C)x refractory high-entropy alloy with excellent mechanical properties. Journal of Alloys and Compounds. 2021;889:161800. https://doi.org/10.1016/j.jallcom.2021.161800

2. Hemphill MA et al. Fatigue behavior of Al0.5CoCrCuFeNi high entropy alloys. Acta Materialia. 2012;60(16):5723–5734. https://doi.org/10.1016/j.actamat.2012.06.046

3. An Z et al. A novel HfNbTaTiV high-entropy alloy of superior mechanical properties designed on the principle of maximum lattice distortion. Journal of Materials Science & Technology. 2021;79:109–117. https://doi.org/10.1016/j.jmst.2020.10.073

4. Gludovatz B et al. A fracture-resistant high-entropy alloy for cryogenic applications. Science. 2014;345(6201):1153–1158. https://doi.org/10.1126/science.1254581

5. Wu YD et al. A refractory Hf25Nb25Ti25Zr25 high-entropy alloy with excellent structural stability and tensile properties. Materials Letters. 2014;130:277–280. https://doi.org/10.1016/j.matlet.2014.05.134

6. El-Atwani O et al. Outstanding radiation resistance of tungsten-based high-entropy alloys. Science Advances. 2002;5(3):eaav2002. https://doi.org/10.1126/sciadv.aav

7. Shi Y, Yang B, Liaw PK. Corrosion-resistant high-entropy alloys: a review. Metals. 2017;7(2):43. https://doi.org/10.3390/met7020043

8. Hsu Y-J, Chiang W-C, Wu J-K. Corrosion behavior of FeCoNiCrCux high-entropy alloys in 3.5% sodium chloride solution. Materials Chemistry and Physics. 2005;92(1):112–117. https://doi.org/10.1016/j.matchemphys.2005.01.001

9. Holcomb GR, Tylczak J, Carney C. Oxidation of CoCrFeMnNi high entropy alloys. JOM. 2015;67(10):2326–233. https://doi.org/10.1007/s11837-015-1517-2

10. Müller F et al. On the oxidation mechanism of refractory high entropy alloys. Corrosion Science. 2019;159:108161. https://doi.org/10.1016/j.corsci.2019.108161

11. Cantor B, Chang ITH, Knight P, Vincent AJB. Microstructural development in equiatomic multicomponent alloys. Materials Science and Engineering: A. 2004;375–377:213–218. https://doi.org/10.1016/j.msea.2003.10.257

12. Snead LL, Hoelzer DT, Rieth M, Nemith AAN. Refractory alloys: vanadium, niobium, molybdenum, tungsten. In: Odette GR, Zinkle SJ, editors. Structural alloys for nuclear energy applications. Elsevier; 2019. Chapter 13. c2019. p. 585–640.

13. Abdullah MR, Peng Z. Review and perspective on additive manufacturing of refractory high entropy alloys. Materials Today Advances. 2024;22:100497. https://doi.org/10.1016/j.mtadv.2024.100497

14. Li C et al. High uniformity of the mechanical properties of arc-melted WNbMoTaZr refractory high entropy alloy. Intermetallics. 2024;167:108213. https://doi.org/10.1016/j.intermet.2024.108213

15. Joshi K, Kumar P. Strength behavior of niobium-based refractory systems. JOM. 2024;76(11):6277–6301. https://doi.org/10.1007/s11837-024-06847-1

16. Yao HW et al. Mechanical properties of refractory high-entropy alloys: experiments and modeling. Journal of Alloys and Compounds. 2017;696: 1139–1150. https://doi.org/10.1016/j.jallcom.2016.11.188

17. Assadi H, Gärtner F, Stoltenhoff T, Kreye H. Bonding mechanism in cold gas spraying. Acta Materialia. 2003;51(15):4379–4394. https://doi.org/10.1016/S1359-6454(03)00274-X

18. Xue K, Guo Y, Shi J, Wei X, Li P. The brittle-to-ductile transition of pure tungsten processed by closed dual equal channel angular pressing process. Materials Science and Engineering: A. 2022;832:142513. https://doi.org/10.1016/j.msea.2021.142513

19. Thornley JC, Wronski AS. The effect of annealing temperature on the ductile-brittle transition temperature of cast molybdenum of constant grain size. Journal of the Less Common Metals. 1970;21(2):205–211. https://doi.org/10.1016/0022-5088(70)90120-7

20. Hussain T. Cold spraying of titanium: a review of bonding mechanisms, microstructure and properties. Key Engineering Materials. 2013;533:53–90. https://doi:10.4028/www.scientific.net/KEM.533.53

21. Binder K, Gottschalk J, Kollenda M, Gärtner F, Klassen T. Influence of impact angle and gas temperature on mechanical properties of titanium cold spray deposits. Journal of Thermal Spray Technology. 2011;20(1):234–242. https://doi.org/10.1007/s11666-010-9557-1

22. Kumar S, Ramakrishna M, Chavan NM, Joshi SV. Correlation of splat state with deposition characteristics of cold sprayed niobium coatings. Acta Materialia. 2017;130:177–195. https://doi.org/10.1016/j.actamat.2017.03.023

23. Van Steenkiste T, Gorkiewicz DW. Analysis of tantalum coatings produced by the kinetic spray process. Journal of Thermal Spray Technology. 2004;13(2):265–273. https://doi.org/10.1361/10599630419418

24. Kim Y-K, Kim H-J, Lee K-A. Solid-state cold spray additive manufacturing of pure tantalum with extraordinary high-temperature mechanical properties. Journal of Materials Research and Technology. 2023;23:5698–5709. https://doi.org/10.1016/j.jmrt.2023.02.184

25. Maier B et al. Development of cold spray chromium coatings for improved accident tolerant zirconium-alloy cladding. Journal of Nuclear Materials. 2019;519:247–254. https://doi.org/10.1016/j.jnucmat.2019.03.039

26. Yeom H et al. Improving deposition efficiency in cold spraying chromium coatings by powder annealing. The International Journal of Advanced Manufacturing Technology. 2019;100(5):1373–1382. https://doi.org/10.1007/s00170-018-2784-1

27. Cold spraying zirconium. Impact Innovations GmbH [accessed 2025 Apr 17]. https://doi.org/impact-innovations.com/en/materials/zirconium/

28. Schindelin J et al. Fiji: an open-source platform for biological-image analysis. Nature Methods. 2012;9(7):676–682. https://doi.org/10.1038/nmeth.2019

29. Paul A, van Dal MJH, Kodentsov AA, van Loo FJJ. The Kirkendall effect in multiphase diffusion. Acta Materialia. 200452(3):623–630. https://doi.org/10.1016/j.actamat.2003.10.007

30. Pavlů J, Vřešťál J, Šob M. Thermodynamic modeling of laves phases in the Cr–Hf and Cr–Ti systems: reassessment using first-principles results. Calphad. 2010;34(2):215–221. https://doi.org/10.1016/j.calphad.2010.03.003

31. Pavlů J, Vřešťál J, Šob M. Stability of laves phases in the Cr–Zr system. Calphad. 2009;33(2):382–387. https://doi.org/10.1016/j.calphad.2008.11.003

32. Rudy E. Compendium of phase diagram data. Air Force Materials Laboratory, Metals and Ceramics Division; 1969.

33. Yin S, Jenkins R, Yan X, Lupoi R. Microstructure and mechanical anisotropy of additively manufactured cold spray copper deposits. Materials Science and Engineering: A. 2018;734:67–76. https://doi.org/10.1016/j.msea.2018.07.096

34. Caplan D, Cohen M. The volatilization of chromium oxide. Journal of the Electrochemical Society. 1961;108(5):438. https://doi.org/10.1149/1.2428106

35. Guo S, Liu CT. Phase stability in high entropy alloys: formation of solid-solution phase or amorphous phase. Progress in Natural Science: Materials International. 2011;21(6):433–446. https://doi.org/10.1016/S1002-0071(12)60080-X

36. Gray T, Whitby M, Mann N. The photographic periodic table of the elements. periodictable.com. 2014 [accessed 2025 May 14].

37. Vasant Kumar R, Chivall J, Brook D, Barber B, Sallows L. The interactive Ellingham diagram. University of Cambridge. 2025 [accessed 2025 Aug 28]. https://www.doitpoms.ac.uk/tlplib/ellingham_diagrams/interactive.php

Appendix. Scanning Electron Microscopy and Energy-Dispersive Spectroscopy Mapping of All Alloys

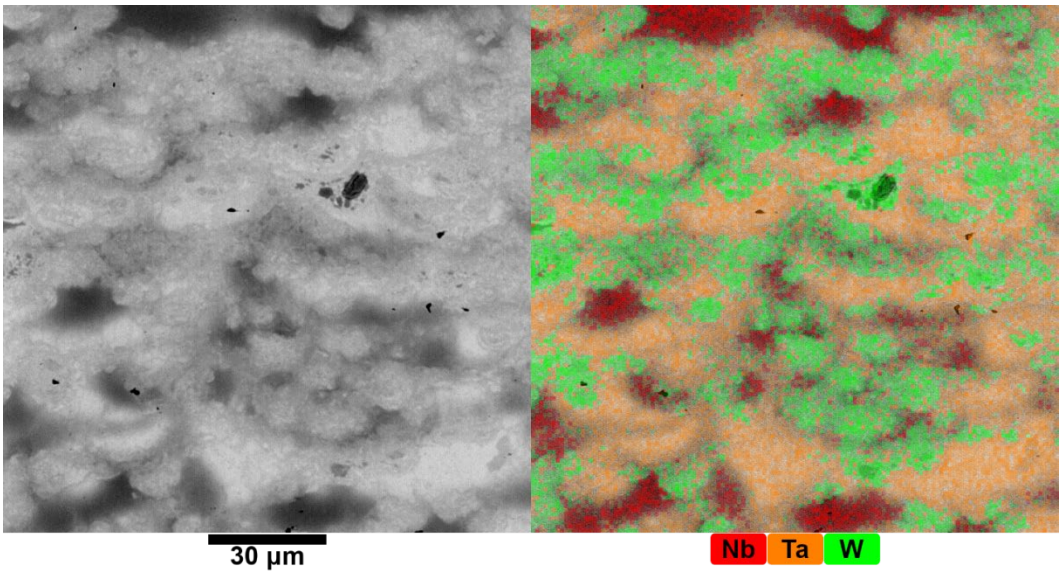

Figure A-1. NbTaW (multiphase).

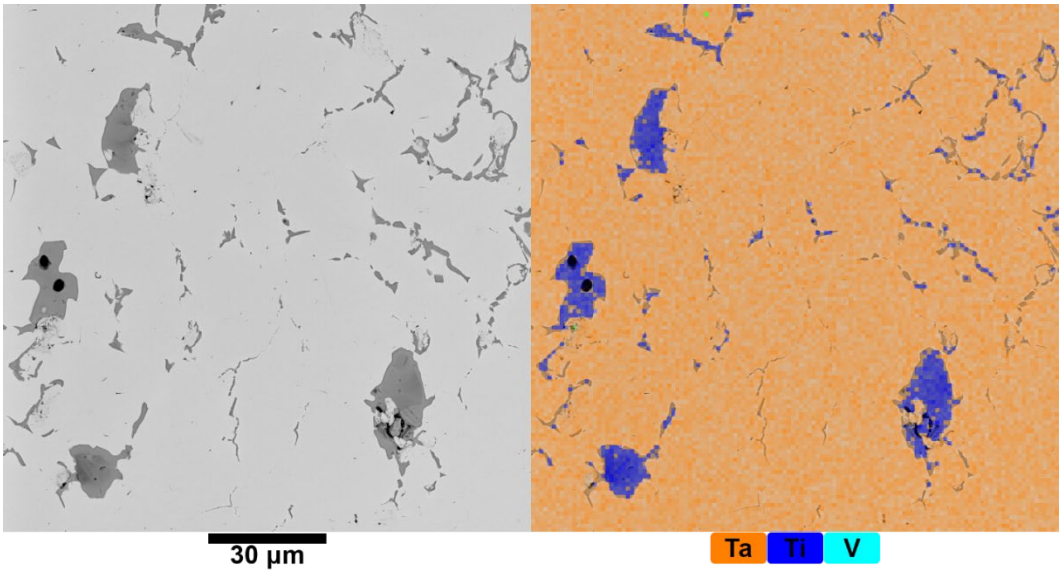

Figure A-2. TaTiV (two-phase).

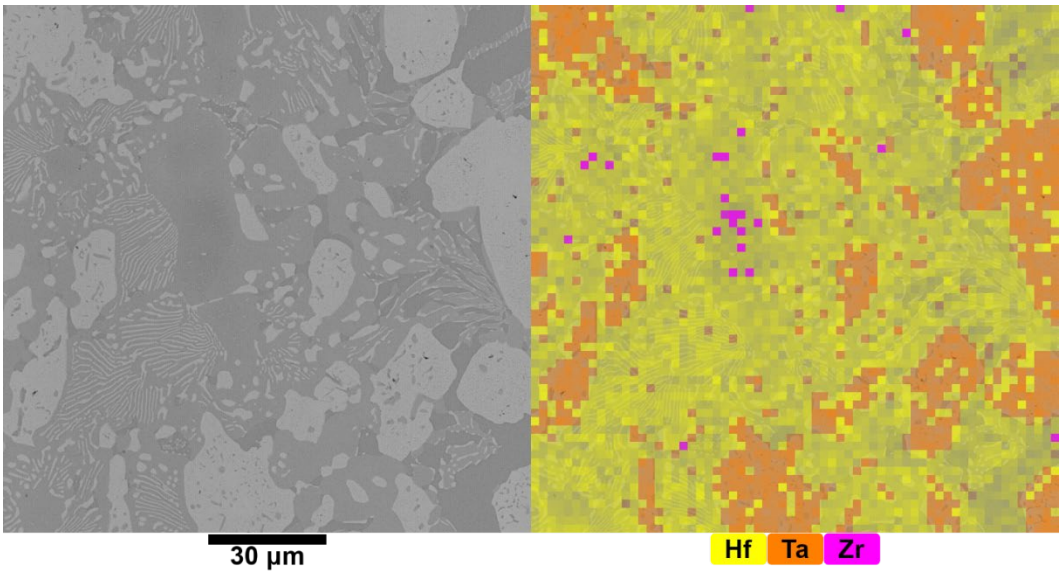

Figure A-3. HfTaZr (two-phase).

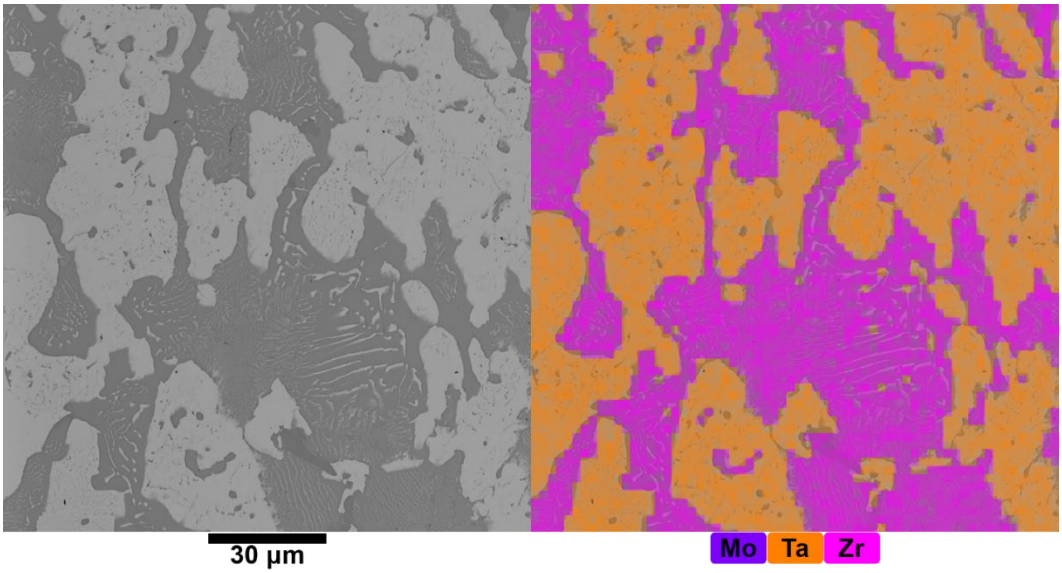

Figure A-4. MoTaZr (two-phase).

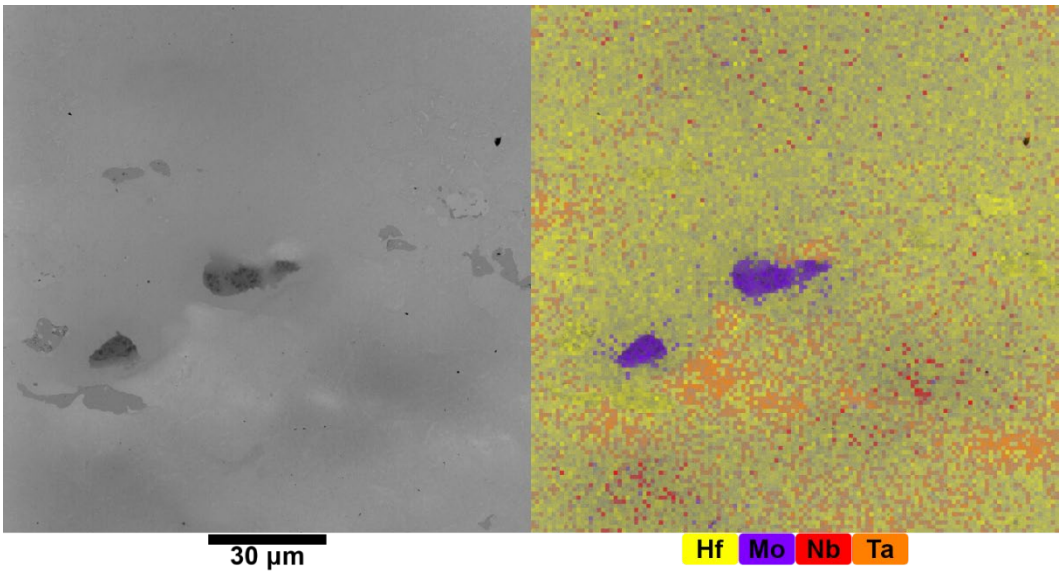

Figure A-5. HfMoNbTa (multiphase).

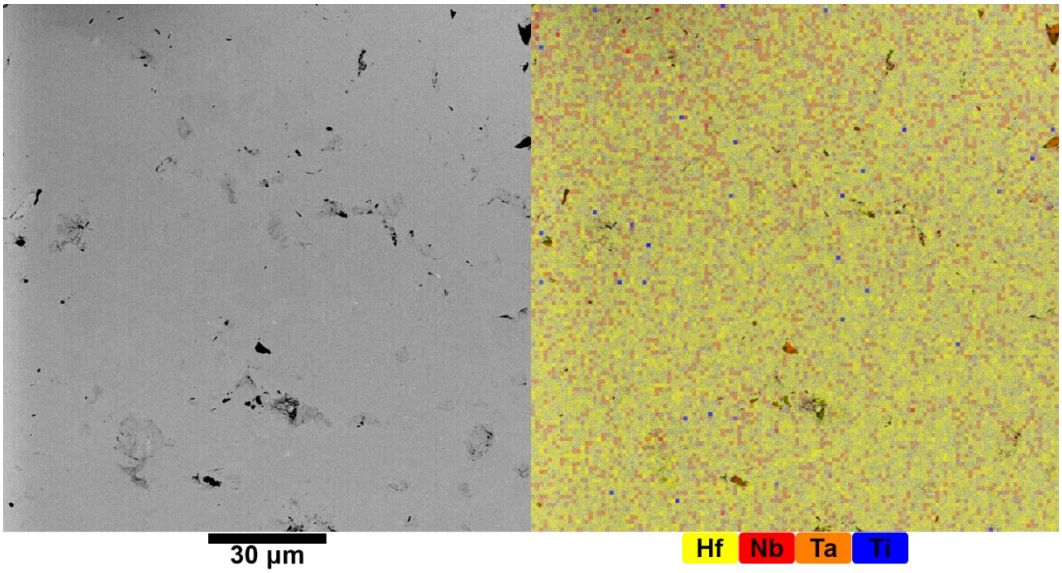

Figure A-6. HfNbTaTi (single-phase).

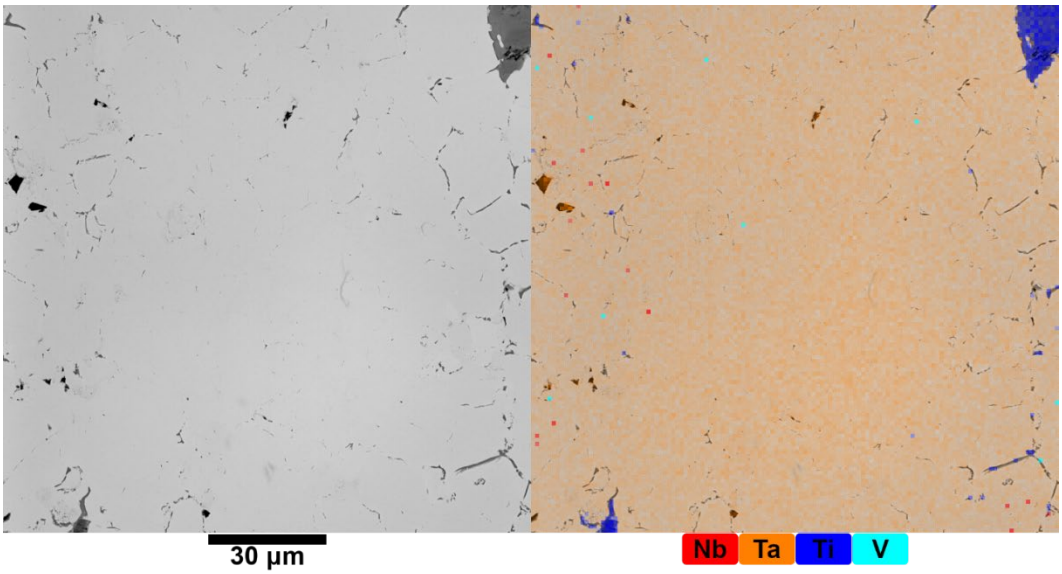

Figure A-7. NbTaTiV (single-phase).

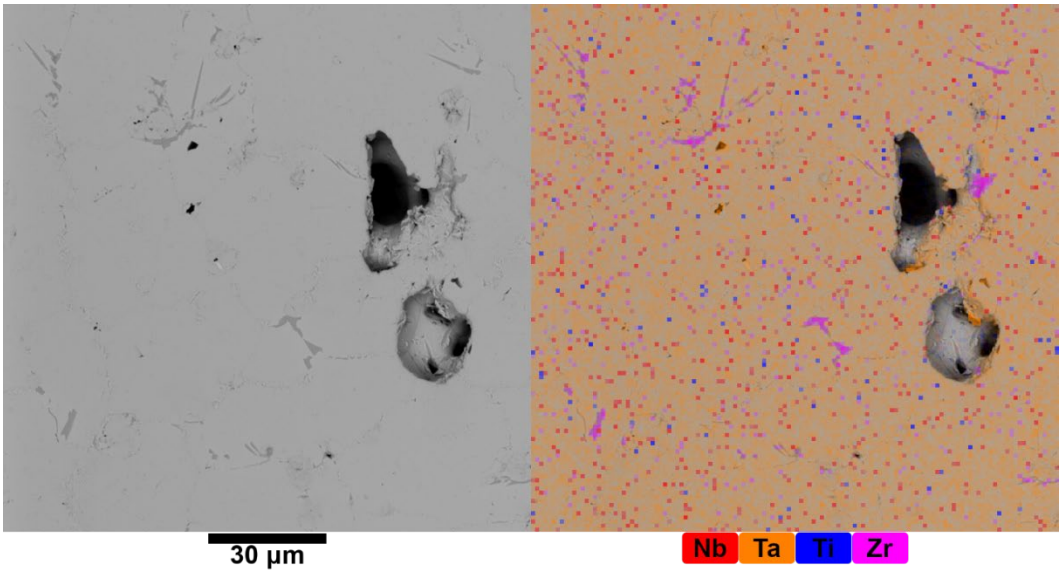

Figure A-8. NbTaTiZr (single-phase).

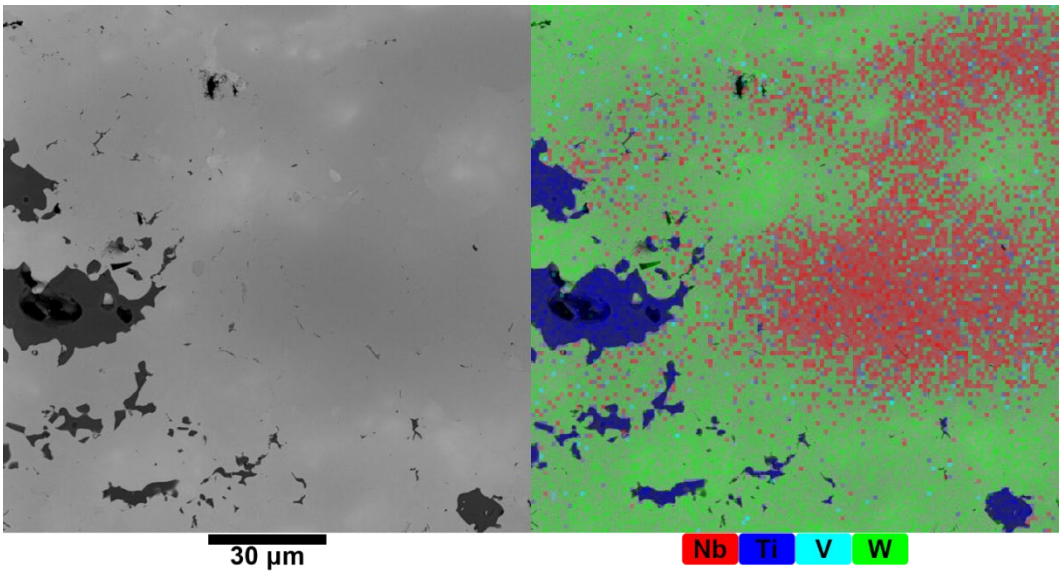

Figure A-9. NbTiVW (multiphase).

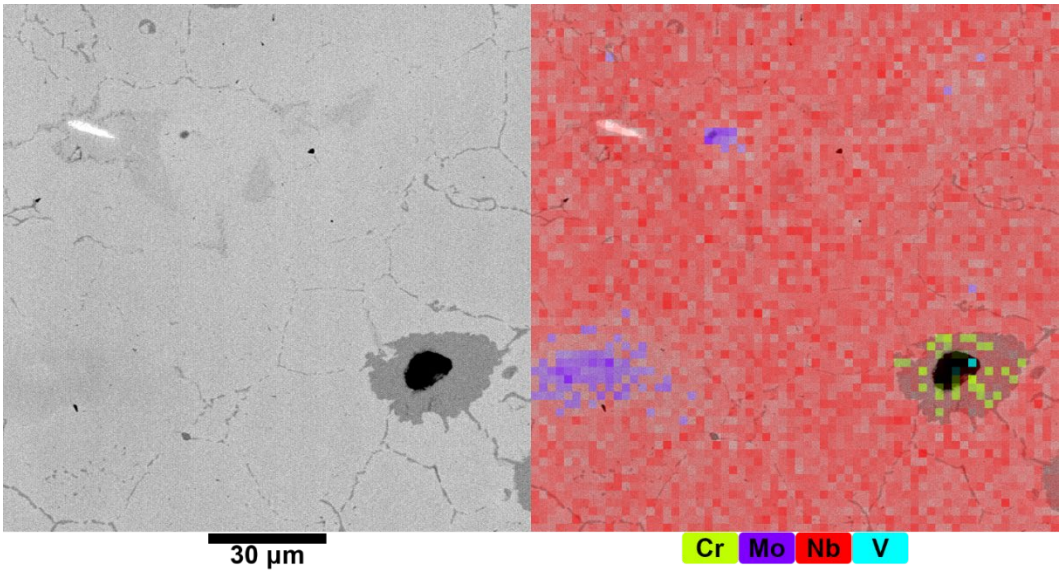

Figure A-10. CrMoNbV (multiphase).

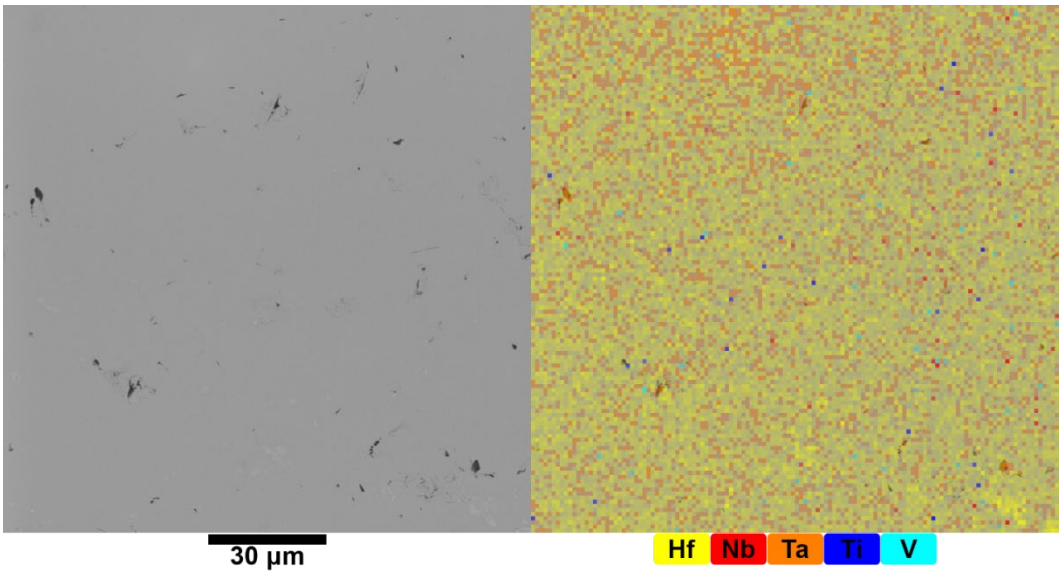

Figure A-11. HfNbTaTiV (single-phase).

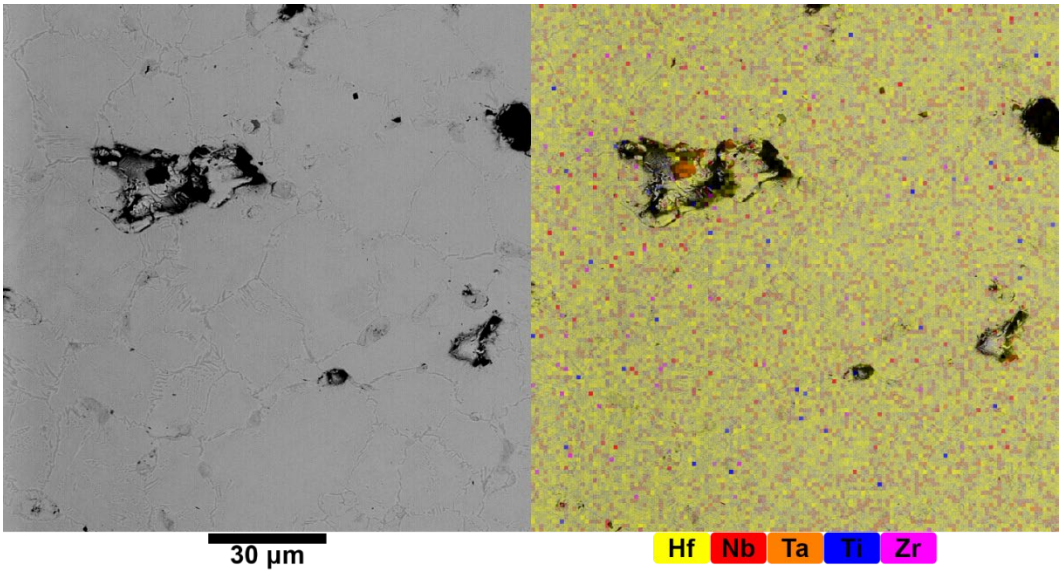

Figure A-12. HfNbTaTiZr (single-phase).

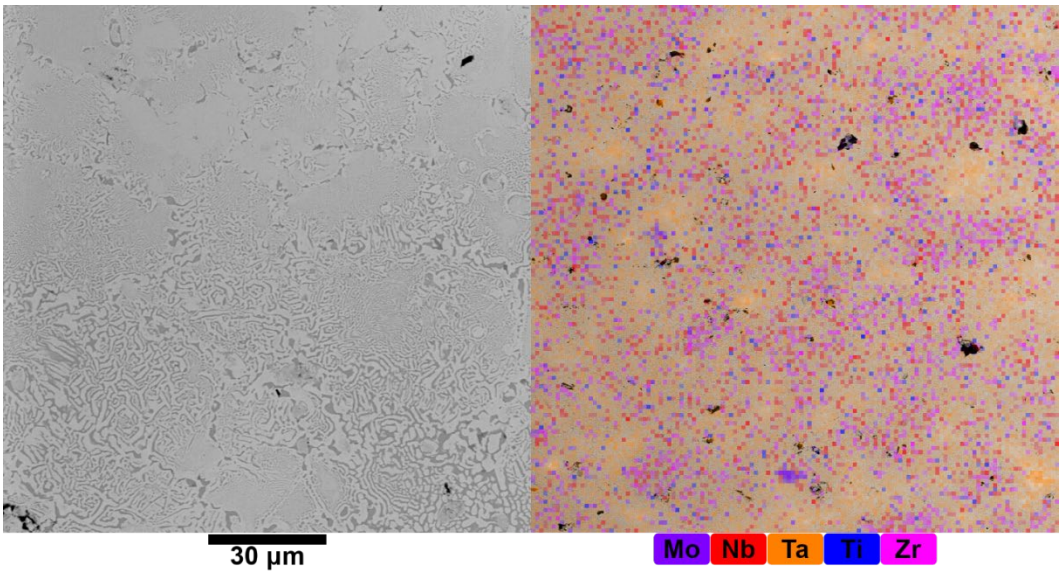

Figure A-13. MoNbTaTiZr (two-phase).

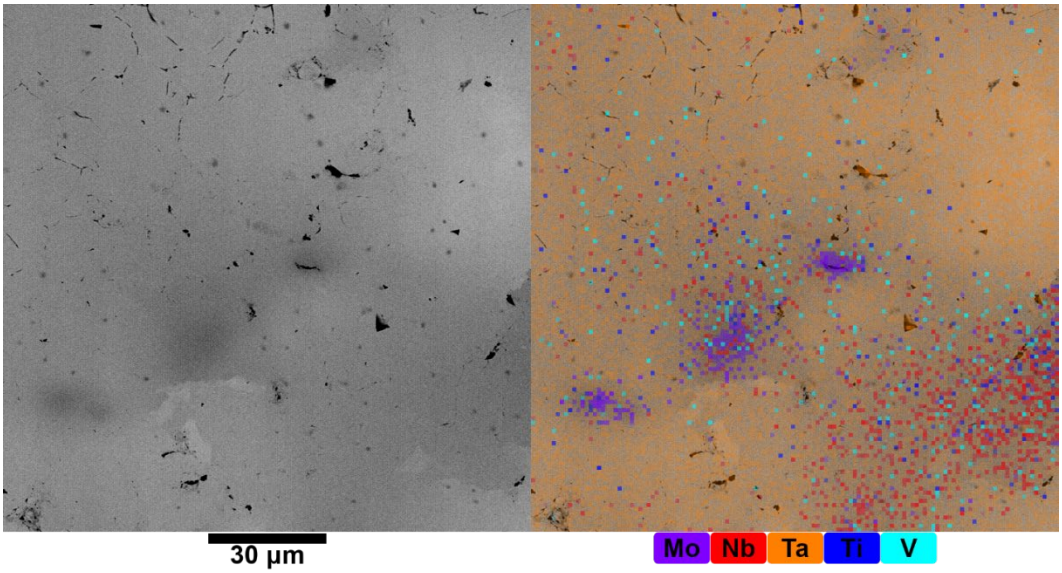

Figure A-14. MoNbTaTiV (multiphase).

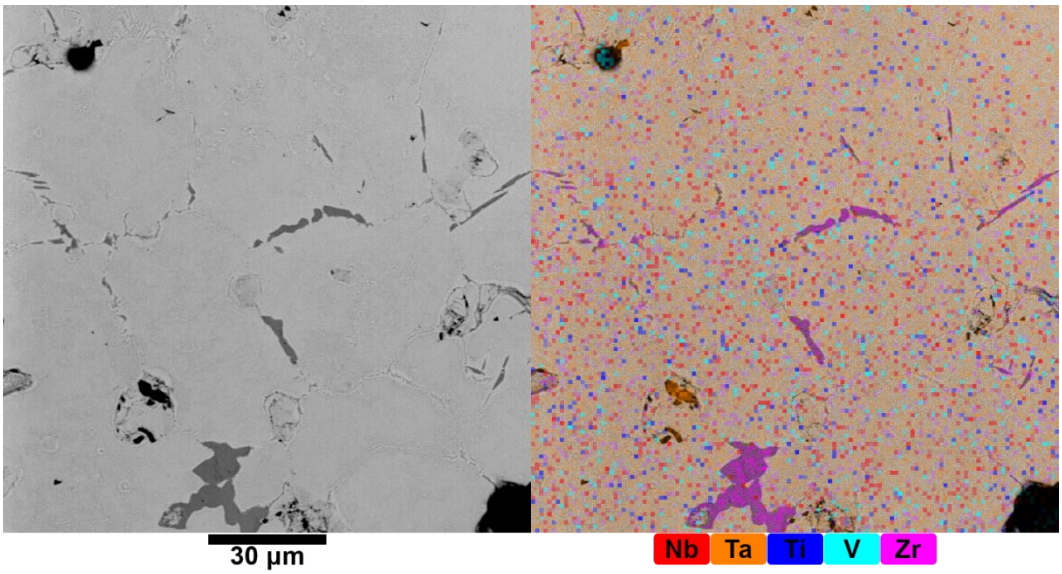

Figure A-15. NbTaTiVZr (two-phase).

List of Symbols, Abbreviations, and Acronyms

Al_2O_3	Alumina
AM	Additive Manufacturing
CS	Cold Spray
CSAM	Cold Spray Additive Manufacturing
EDS	Energy-Dispersive Spectroscopy
HEA	High-Entropy Alloy
HfO_2	Hafnium Oxide
RHEA	Refractory High-Entropy Alloy
SEM	Scanning Electron Microscopy
ZrO_2	Zirconium Dioxide

1 (PDF)	DEFENSE TECHNICAL INFORMATION CTR DTIC OCA
1 (PDF)	DEVCOM ARL FCDD RLB CI TECH LIB